nature geoscience
SUPPLEMENTARY INFORMATION
DOI: 10.1038/NGEO855

Mantle upwellings

above slab graveyards linked to the global geoid lows

SUPPLEMENTARY MATERIAL

Sonja Spasojevic[1], Michael Gurnis[1] and Rupert Sutherland[2]

[1]Seismological Laboratory, California Institute of Technology, Pasadena, CA 91125, USA

[2]GNS Science, PO Box 30368, Lower Hutt 5040, New Zealand

DOI: 10.1038/NGEO855

Supplementary Figure S1. Details of velocity structure for models S20RTS[1] (first column) and SB4L18[2] (second column), and model TX2005[3] (third column) in the zones of geoid minima. (a) Integrated tomography in depth range 2050-2850 km; (b) Integrated tomography in depth range 300-1000 km; (c) Cross section from North America to Ross Sea; (d) Cross section from central Asia to Ross Sea; (e) Correlation coefficient between observed geoid and tomography calculated at every 100 km depth; (f) Observed geoid. Semi-transparent outlines on (a-b) cover zone of global geoid high; blue and red dashed lines (c-d) indicate lower mantle high velocity and upper-to-mid mantle low velocity anomalies of interest, respectively; black, blue and red lines on (e) show mean correlation coefficient between whole geoid, areas of negative geoid and areas of positive geoid, respectively; red lines on (f) indicate position of great circle cross-sections intersecting geoid low. Correlation coefficient between observed geoid and tomography models (e) is calculated as a product of values divided by product of standard deviations at every 100 km depth. The mean value of correlation coefficient is than calculated for whole geoid, areas of geoid lows, and geoid highs.

Integrated tomography plots (a-b) show a correlation between geoid low (f) and both seismically fast regions in lower mantle (a) and slow regions in upper-to-mid mantle (b) for all investigated tomography models. In the region of NE Pacific geoid low, all models define a seismically fast anomaly in the lower 500-1000 km of mantle (c), which is probably related to an ancient subducted slab that hasn't been recognized previously, except by analysis of SKS-SKKS splitting discrepancies[4]. A zone of upper-mid mantle seismically slow velocities is located above this fast anomaly (c), model SB4L18[2] defines this structure largely in the lower mantle, while models S20RTS[1] and TX2005[3] place it at depths up to 800 km. In the Ross Sea region (c-d), all models show coherent upper-mid mantle seismically slow region. Fast seismic anomaly in the lower mantle appears to consist of several separate structures, possibly corresponding to different stages of Gondwana subduction. In the zone of Indian Ocean geoid low, all models clearly define fast seismic anomalies in the lower mantle (d), that was previously attributed to Mesozoic Tethyan subduction[5]. In the upper-to-mid mantle, TX2005 defines the most coherent slow region in depth range of 300-800 km (d) in the region of local geoid low (10°S to 10°N), while models S20RTS and SB4L18 show no particularly distinctive region of slow velocities (d). Correlation analysis between observed geoid tomography and various component of geoid (e) indicate that negative geoid is correlated with low velocity tomographic anomalies in upper 1200-1500 km of mantle and high velocity seismic anomalies in the lower mantle. Positive geoid is correlated with high velocity anomalies in upper 800 km of mantle and negative seismic anomalies in the lower mantle.

 DOI: 10.1038/NGEO855

Supplementary Figure S2. Details of viscosity structure. (a) Tectonic regionalization map with high viscosity cratons, low viscosity mantle wedges and intermediate viscosity background regions; (b) S20RTS tomography at 250 km depth with outlines (green) of geologically defined cratons[6]; (c) Radial viscosity structure for models with tectonic regionalization; (d) Radial viscosity structure for models without tectonic regionalization; (e-f) Viscosity cross-sections for models with (e) and without (f) tectonic regionalization; (g) Global temperature cross-section; (h) Regional cross-section through NE Pacific geoid low with velocity vectors overlay. Position of cross-sections (e-h) is shown with black line on (a); red, green and blue rectangles on (c) show upper mantle range of viscosities for cratons, background and wedges, respectively; grey rectangles on (c-d) show range of viscosities in lower and upper mantle.

Following the experience from previous studies that use scaled tomographic models for geoid and gravity predictions to either define only the best fitting radial viscosity structure[7,8,9,10,11], without imposing any lateral tectonic viscosity parameterization, or models in which viscosity is not just a function of depth and temperature (seismic velocity), but also have pre-imposed large-scale variations based on upper mantle structure and tectonics[12,13,14,15], we develop two types of models: (1) models with tectonic regionalization in the upper mantle (a-c, e), and (2) models without tectonic regionalization in the upper mantle (d, f). For models with tectonic regionalization, high viscosity cratons are defined simultaneously using seismic tomographic maps[2,3,16] in the depth range 200-250 km and geologically defined cratonic outlines[6] (b), including spatially more extensive area of the two in each particular region. The high viscosity cratons in our models (a) are more extensive than geologically defined cratons (b) and often include several neighboring geologically defined cratonic regions (a), as our models have a wide (~1000 km where possible) regions of interpolations toward the neighboring regions, and merge a number of geologically defined cratonic areas (a). The Australian cratonic region (a) is extended in a way that high-viscosity province also encompasses the Australia-Antarctic discordance zone (AAD), as we were unable to reproduce the correct sign of geoid without AAD having high viscosity in upper mantle. Mantle viscosity wedges are defined as ~1000 km wide zones of lower viscosities that extend from the trench into the backarc region (a), with wider regions defined in the regions of multiple neighboring subduction zones with opposite polarities, such as ones in the SW Pacific (a). We vary viscosity values in depth range 100-250 km in the tectonically regionalized model as it follows: cratons 10^{21}- 10^{22} Pa s, mantle wedges 10^{18}-10^{19} Pa s, background regions 10^{20}- 10^{21} Pas. Viscosity of the mantle in depth range 250-660 km is kept constant (10^{21} Pas), while the lower mantle viscosity is varied between 10^{22} and 10^{23} Pas. For the models without tectonic regionalization, we adopt 4-layer viscosity structure (d, f) that consists of: lithosphere (viscosity 10^{24} Pas), upper mantle (viscosity varied between 10^{19} and 10^{21} Pas), transition zone (viscosity 10^{21} Pas), and lower mantle (viscosity varied between 10^{22} and 10^{23} Pas). Temperature-dependent viscosity is used for both types of viscosity parameterization (e-f).

DOI: 10.1038/NGEO855

Supplementary Figure S3. Geoid predictions for different viscosity models and a constant seismic velocity- density scaling. (a-b) Models with imposed tectonic regionalization; (c-e) Models without tectonic regionalization; (f) Observed geoid;, (g) Seismic velocity- density scaling used for models (a-e). First, second and third columns show models with viscosity increase between transition zone and lower mantle of 1:20, 1:60 and 1:100, respectively. Fourth column shows details of radial viscosity structure. All buoyancy anomalies are defined from S20RTS tomography[1]. C1 represents correlation coefficient between observed and predicted geoid for whole Earth's surface, and C2 indicates average correlation coefficient in the zones of geoid low.

For models with tectonic regionalization (a-b), low viscosity ratio between transition zone and lower mantle (1:20) always results in geoid prediction that is dominated by degree-2 pattern. High viscosity ratios across 660 km discontinuity of 1:60 to 1:100 yield more realistic predictions for the models with imposed tectonic regionalization (a-b). Lower viscosity of mantle wedges (b) of 10^{18} Pa s results in more positive geoid anomaly in the present-day subduction zones, comparing to higher mantle wedge viscosity of 10^{19} Pa s (a), suggesting that the mantle viscosity wedge could be significantly lower that the surrounding regions. For the models without tectonic regionalization, all models with high viscosity of upper mantle (depth range 100-410 km) yield geoid prediction dominated by degree-2 pattern (c), indicating that upper mantle viscosity has to be lower than 10^{21} Pa s. Models with upper mantle viscosity of 10^{20} Pa s and transition zone viscosity of 10^{21} Pa s (d) yield good predictions of geoid for viscosity ratios across 660 km discontinuity larger than 1:60. Finally, if viscosity of the upper mantle is reduced to

10^{19} Pa s (e) predicted geoid patterns are reasonable just for low (1:20 or lower) ratio of transition zone: lower mantle viscosity, but the predicted geoid amplitudes are too high.

 DOI: 10.1038/NGEO855

Supplementary Figure S4. Comparison of geoid prediction for models utilizing S20RTS[1], SB4L18 [2] and TX2005[3] tomography models. (a) Geoid predictions centered on Pacific hemisphere; (b) Observed geoid[17] centered on Pacific hemisphere; (c) Seismic velocity-density scaling; (d) Geoid predictions centered on Atlantic hemisphere; (e) Observed geoid centered on Atlantic hemisphere[17], (f) Radial viscosity profile. Ratios 1:40, 1:80 and 1:100 indicate viscosity increase between transition zone and lower mantle. Negative buoyancy in upper mantle is defined based on RUM model[18], while other buoyancy anomalies are defined using seismic velocity- density scaling shown on (c). C1 represents correlation coefficient between observed and predicted geoid for whole Earth's surface, and C2 indicates average correlation coefficient in the zones of geoid low.

For all models, the preferred viscosity ratio across 660 km has to be higher than 1:40, as models with this viscosity ratio have geoid predictions mostly dominated by degree-2 pattern (a, d). For the Pacific and circum-Pacific region, three models yield rather different geoid predictions (a). Models SB4L18[2] and TX2005[3] have more strongly defined central Pacific geoid highs, which relates to stronger tomographic anomaly from the Pacific superplume in the lower mantle (a). Model S20RTS[1] has geoid high translated toward the western Pacific subduction zones, which is more similar to the observations (b). Models SB4L18 and TX2005 are less successful reproducing NE Pacific geoid low, and we therefore prefer model S20RTS for the Pacific region geoid predictions. In addition, predictions of the Ross sea and South Pacific geoid lows are the best obtained by S20RTS model (a). On other hand, S20RTS and SB4L18 models fail reproducing amplitudes of geoid low in the belt extending from Siberia to the Indian Ocean, while

TX2005 is more successful in the geoid low prediction in this region. In the region of Atlantic-Africa geoid highs (d), the SB4L18 model seems to be most successful in predicting geoid trends, with two highs centralized in South Africa (presumably related to the African superplume) and Mediterranean-North Atlantic regions (presumably related to Mediterranean subduction and Iceland hotspot). Model S20RTS is less successful reproducing geoid highs in North Atlantic, and South Africa geoid high predicted further north in the central Africa than observed. Model TX2005 on other hand relatively successfully predicts South Africa geoid high, but it fails to adequately reproduce North Atlantic high (d). Since we are mostly interested in the circum-Pacific belt of geoid lows, we utilized S20RTS model for most of the results shown in the main manuscript.

 DOI: 10.1038/NGEO855

Supplementary Figure S5. Geoid predictions (a-g) for models with different tomography-density scaling functions (i). Observed geoid is shown on (h), colored lines on (i) show scaling functions. Dotted and dashed black lines show range of scaling values suggested by geodynamic (dotted) and mineral physics studies (dashed), based on [19]. All buoyancy anomalies are defined from S20RTS tomography[1]. C1 represents correlation coefficient between observed and predicted geoid for whole Earth's surface, and C2 indicates average correlation coefficient in the zones of geoid low.

Although we significantly vary depth-dependent seismic velocity- density scaling, difference in the geoid prediction is smaller than when viscosity model (Supplementary Fig. S3) or seismic model (Supplementary Fig. S4) are varied. For example, the model with constant scaling of 0.2 (b) yields similarly well-predicted geoid as some of more complex scaling functions (e.g. d, f).

Supplementary Figure S6. Impact of lateral and vertical resolution on geoid prediction for two models without tectonic regionalization (a-b) having different radial viscosity structure (c) and same seismic velocity- density scaling (d). First and second column show geoid predictions centered on Pacific and African hemisphere, respectively. Third column shows predicted dynamic topography. CitcomS global models use 12 caps for the whole globe, and the resolution is defined for each cap. We test two different lateral resolutions: 129x129 (approximately 50 km) and 257x257 (approximately 25 km). In the radial directions we test two resolutions: 65 nodes (approximately 44 km) and 129 nodes in the whole mantle (approximately 22 km), with nodes uniformly distributed in the radial direction. All buoyancy anomalies are defined from S20RTS tomography[1].

We find a slight difference (a-b) in geoid predictions between models that have different vertical resolution (129x129x65 vs. 129x129x129), while there seems to be no difference in geoid prediction between models that have 22 km vertical resolution and different lateral resolution (129x129x129 vs. 257x257x129). However, all patterns and trends of geoid predictions are essentially the same for all resolutions we tested. We attribute the difference in the geoid prediction between models having 44 km and 22 km resolution to the slightly different density/temperature models used as input data. Namely, the higher radial resolution models essentially sample tomography at two times denser interval, therefore introducing slightly different additional content in the density field, which is reflected in the geoid prediction.

 DOI: 10.1038/NGEO855

Supplementary Table 1. Comparison of observed and model geoid minima

	Northeast Pacific			West Atlantic			Indian Ocean			Ross Sea		
	Lon. ° E	Lat. ° N	Amp. m	Lon. ° E	Lat. ° N	Amp. m	Lon. ° E	Lat. ° N	Amp. m	Lon. ° E	Lat. ° N	Amp. m
Observed*	239	22	-46	295	23	-52	78	3	-102	188	-72	-63
							107	-32	-38			
Model A	224	41	-69	310	23	-47	96	-22	-75	186	-58	-75
										252	-49	-52
Model B	224	45	-45	307	22	-45	95	-19	-65	180	-58	-48
										225	-69	-42
										261	-50	-43
Model C	265	11	-26	306	22	-29	88	-7	-63	170	-59	-28
				311	-11	-32				264	-58	-39

*Filtered to remove features <1000 km in size.

Note: The Hudson Bay anomaly is not compared due to its partial glacial rebound origin.

Supplementary Table 1 shows amplitudes of observed and model geoid minima for the preferred model (Fig. 2), obtained for viscosity structure shown on Fig. 3b (viscosity ratio at 660 km is 1:100) and seismic velocity-to-density scaling shown on Fig. 3g. Model A corresponds to the best-fitting model shown on Fig. 2a, while models B and C correspond to the models shown on Figs. 2b-c, having upwellings removed from the best-fitting model from depths 0-660 km (B) and 0-1000 km (C). Amplitudes of geoid minima are evaluated at the several locations for observed and predicted models, with the coordinates shown in the table and general location of the zones of localized geoid lows shown on Fig. 2a-d. There is a good agreement between observed and predicted geoid amplitudes for the best fitting model (Model A; Fig. 2a). Once the upwellings are removed from the upper mantle (Model B, Fig. 2b) and 0-1000 km depth (Model C, Fig. 2c), the amplitude fit becomes worse.

DOI: 10.1038/NGEO855

Supplementary Table S2. Model parameters held constant in our runs.

Parameter	Symbol	Value
Ambient mantle density	ρ_m	3340 kg/m^3
Reference viscosity	η_o	1x10^{21} Pa s
Thermal diffusivity	κ	10^{-6} m^2/s
Coefficient of thermal expansion	α	3x10^{-5} 1/K
Gravitational acceleration	g	9.81 m/s^2
Earth's radius	R	6371 km
Rayleigh number	Ra	7.5x10^7

References:

1 Ritsema, J., van Heijst, H. J. & Woodhouse, J. H. Global transition zone tomography. *Journal of Geophysical Research-Solid Earth* **109**, doi:10.1029/2003jb002610 (2004).

2 Masters, G., Laske, G., Bolton, H. & Dziewonski, A. The relative behavior of shear velocity, bulk sound speed, and compressional velocity in the mantle: Implications for chemical and thermal structure: *Geophysical Monograph Series* **117** (eds SI Karato *et al.*), 63-88 (American Geophysical Union, 2000).

3 Simmons, N. A., Forte, A. M. & Grand, S. P. Constraining mantle flow with seismic and geodynamic data: A joint approach. *Earth Planet. Sci. Lett.* **246**, 109-124, doi:10.1016/j.epsl.2006.04.003 (2006).

4 Long, M. Complex anisotropy in D beneath the eastern Pacific from SKSñSKKS splitting discrepancies. *Earth Planet. Sci. Lett.* **283**, 181-189 (2009).

5 Van der Voo, R., Spakman, W. & Bijwaard, H. Tethyan subducted slabs under India. *Earth Planet. Sci. Lett.* **171**, 7-20 (1999).

6 Stoddard, P. R. & Abbott, D. Influence of the tectosphere upon plate motion. *Journal of Geophysical Research-Solid Earth* **101**, 5425-5433 (1996).

7 Steinberger, B. Slabs in the lower mantle - results of dynamic modelling compared with tomographic images and the geoid. *Phys. Earth Planet. Inter.* **118**, 241-257 (2000).

8 Steinberger, B. & Calderwood, A. R. Models of large-scale viscous flow in the Earth's mantle with constraints from mineral physics and surface observations.

Geophysical Journal International **167**, 1461-1481, doi:10.1111/j.1365-246X.2006.03131.x (2006).

9 Forte, A. M. & Mitrovica, J. X. Deep-mantle high-viscosity flow and thermochemical structure inferred from seismic and geodynamic data. *Nature* **410**, 1049-1056 (2001).

10 Forte, A. M. in *Treatise of Geophysics* Vol. 1 eds B. Romanowicz & A.M. Dziewonski) 805-854 (2007).

11 Simmons, N. A., Forte, A. M. & Grand, S. P. Joint seismic, geodynamic and mineral physical constraints on three-dimensional mantle heterogeneity: Implications for the relative importance of thermal versus compositional heterogeneity. *Geophysical Journal International* **177**, 1284-1304, doi:10.1111/j.1365-246X.2009.04133.x (2009).

12 Yoshida, M. & Nakakuki, T. Effects on the long-wavelength geoid anomaly of lateral viscosity variations caused by stiff subducting slabs, weak plate margins and lower mantle rheology. *Phys. Earth Planet. Inter.* **172**, 278-288, doi:10.1016/j.pepi.2008.10.018 (2009).

13 Yoshida, M. Possible effects of lateral viscosity variations induced by plate-tectonic mechanism on geoid inferred from numerical models of mantle convection. *Phys. Earth Planet. Inter.* **147**, 67-85, doi:10.1016/j.pepi.2004.06.011 (2004).

14 Cadek, O. & Fleitout, L. Effect of lateral viscosity variations in the top 300 km on the geoid and dynamic topography. *Geophysical Journal International* **152**, 566-580 (2003).

15 Kaban, M. K., Rogozhina, I. & Trubitsyn, V. Importance of lateral viscosity variations in the whole mantle for modelling of the dynamic geoid and surface

velocities. *Journal of Geodynamics* **43**, 262-273, doi:10.1016/j.jog.2006.09.020 (2007).

[16] Ritsema, J. & van Heijst, H. J. Seismic imaging of structural heterogeneity in Earth's mantle: Evidence for large-scale mantle flow. *Science Progress* **83**, 243-259 (2000).

[17] Förste, C. *et al.* The GeoForschungsZentrum Potsdam/Groupe de Recherche de Geodesie Spatiale satellite-only and combined gravity field models: EIGEN-GL04S1 and EIGEN-GL04C. *J. Geodesy* **82**, 331-346, doi:10.1007/s00190-007-0183-8 (2008).

[18] Gudmundsson, O. & Sambridge, M. A regionalized upper mantle (RUM) seismic model. *Journal of Geophysical Research-Solid Earth* **103**, 7121-7136 (1998).

[19] Karato, S. & Karki, B. B. Origin of lateral variation of seismic wave velocities and density in the deep mantle. *Journal of Geophysical Research-Solid Earth* **106**, 21771-21783 (2001).

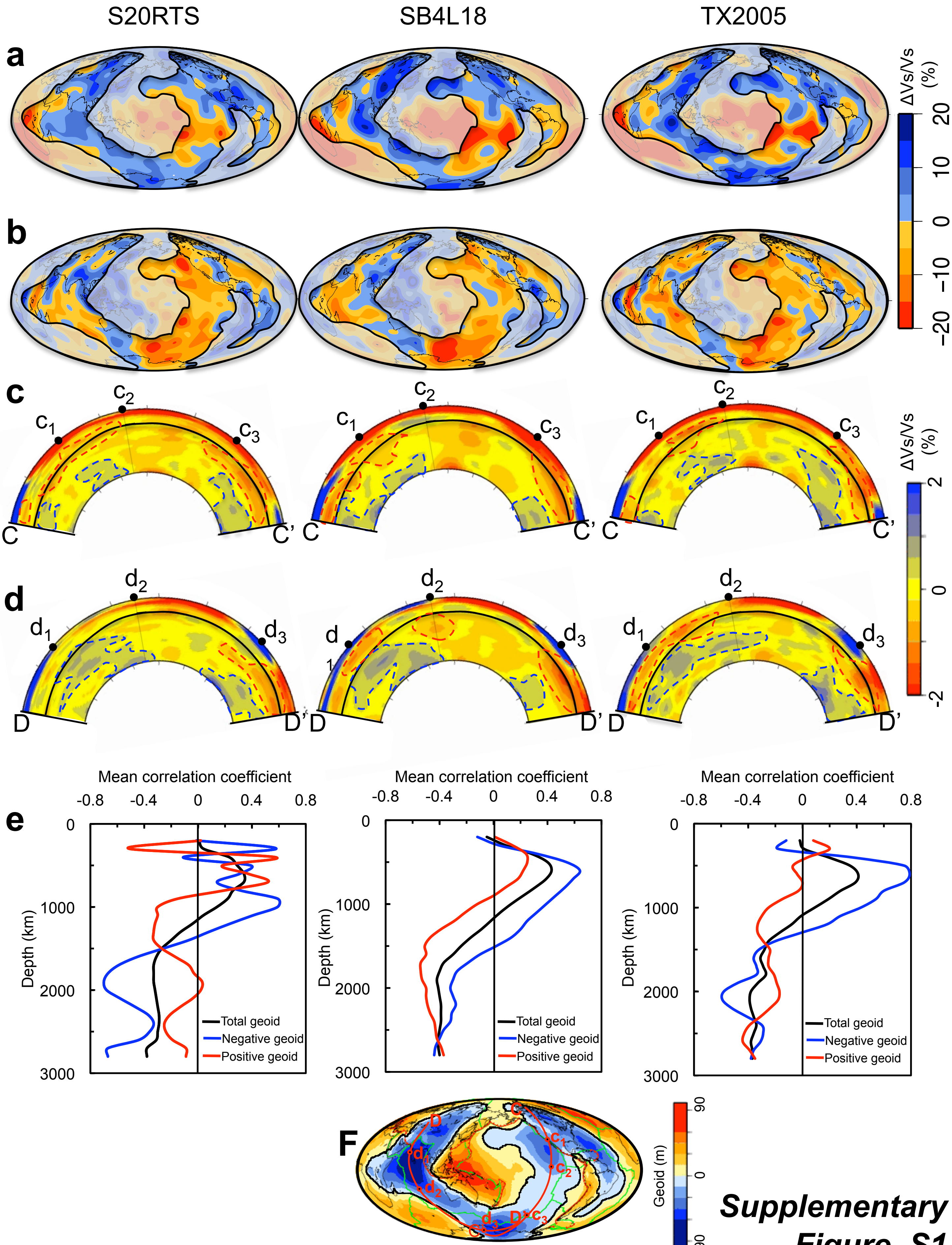

Supplementary Figure S1

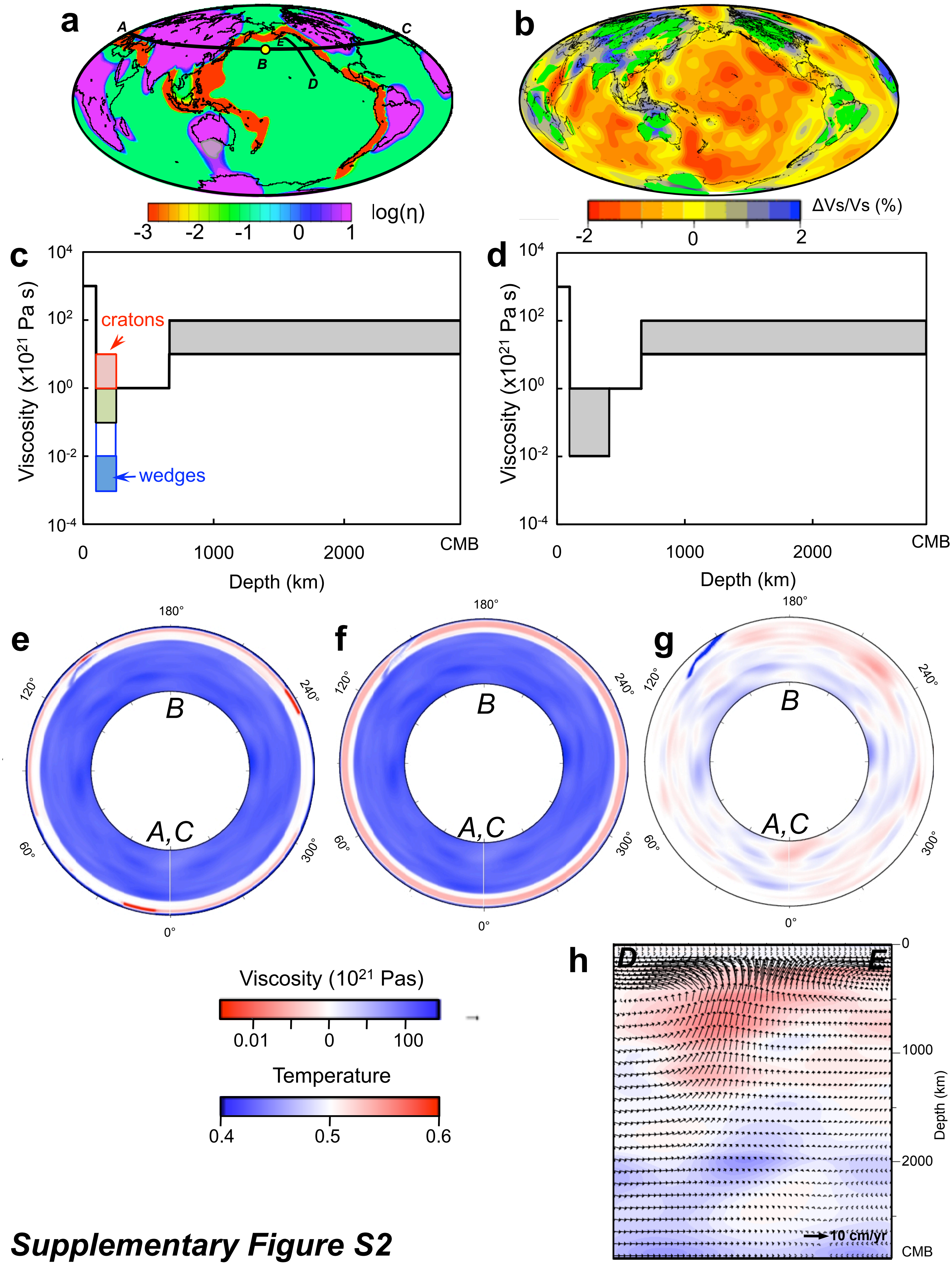

Supplementary Figure S2

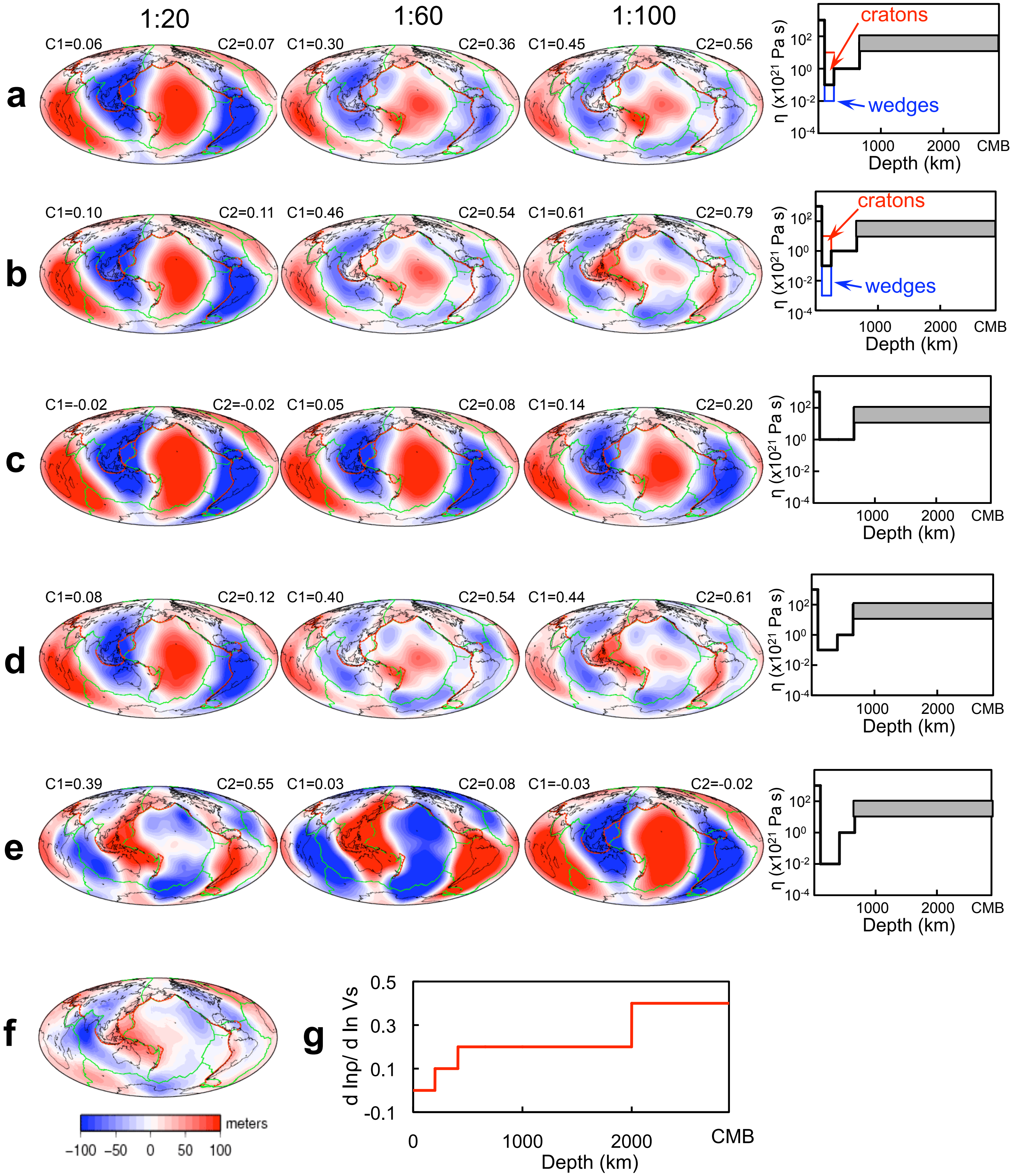

Supplementary Figure S3

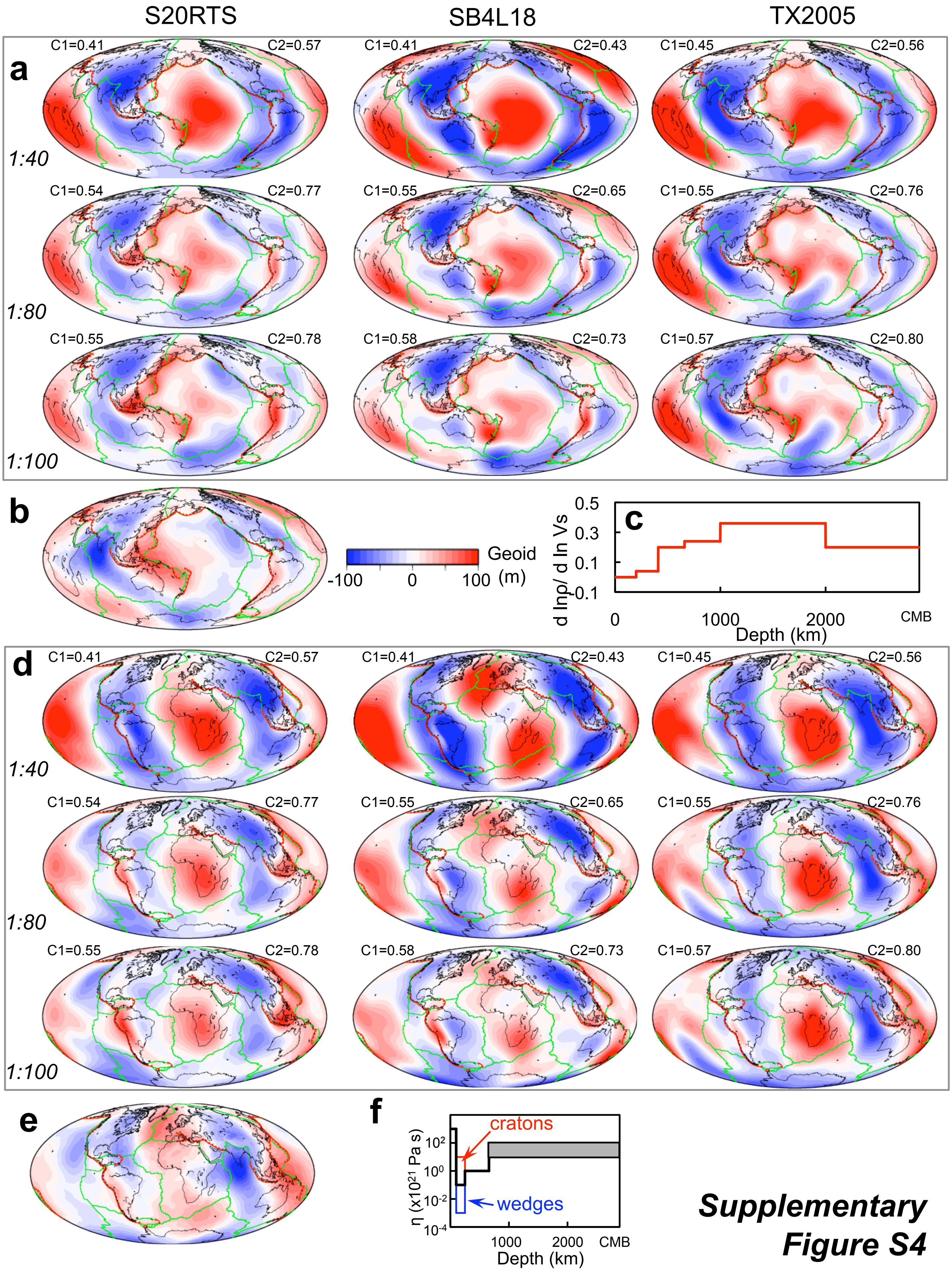

Supplementary Figure S4

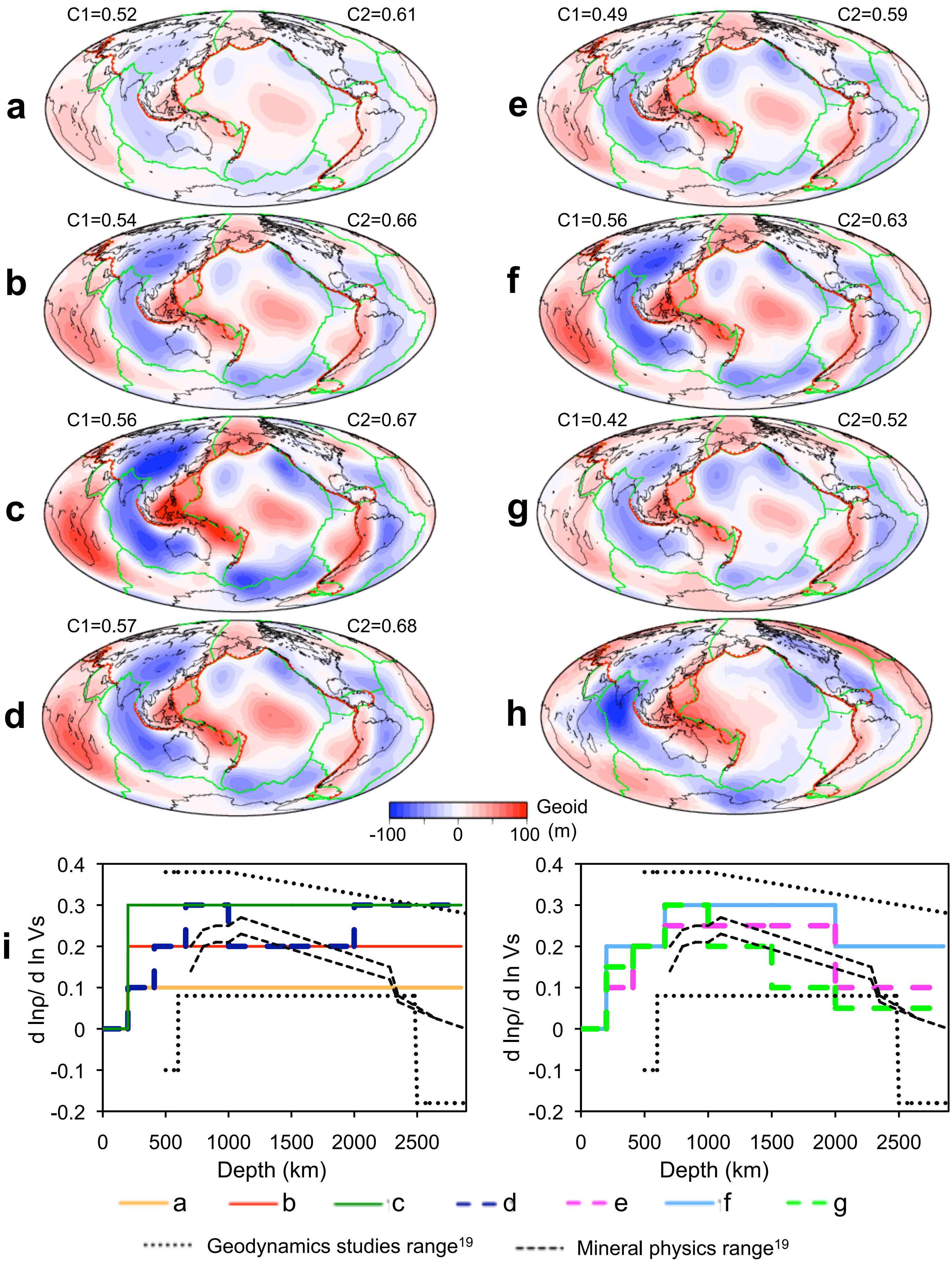

Supplementary Figure S5

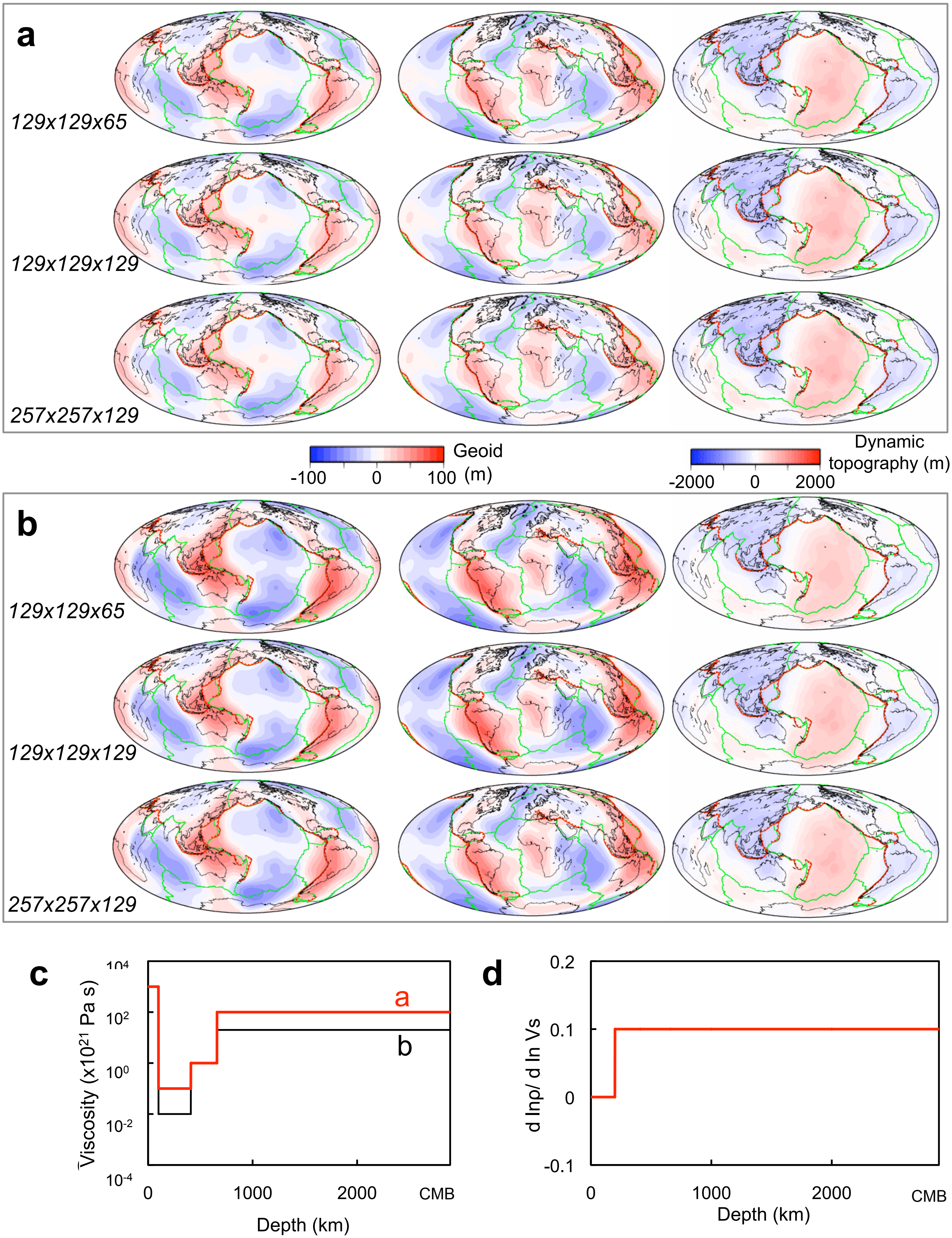

Supplementary Figure S6